

REPORT DOCUMENTATION PAGE

Form Approved
OMB No. 0704-0188

Public reporting burden for this collection of information is estimated to average 1 hour per response, including the time for reviewing instructions, searching existing data sources, gathering and maintaining the data needed, and completing and reviewing this collection of information. Send comments regarding this burden estimate or any other aspect of this collection of information, including suggestions for reducing this burden to Department of Defense, Washington Headquarters Services, Directorate for Information Operations and Reports (0704-0188), 1215 Jefferson Davis Highway, Suite 1204, Arlington, VA 22202-4302. Respondents should be aware that notwithstanding any other provision of law, no person shall be subject to any penalty for failing to comply with a collection of information if it does not display a currently valid OMB control number. **PLEASE DO NOT RETURN YOUR FORM TO THE ABOVE ADDRESS.**

| | | | | | |
|---|------------------------------------|---|--|--|---|
| 1. REPORT DATE (DD-MM-YYYY) | | 2. REPORT TYPE Technical Papers | | 3. DATES COVERED (From - To) | |
| 4. TITLE AND SUBTITLE | | | | 5a. CONTRACT NUMBER | |
| | | | | 5b. GRANT NUMBER | |
| | | | | 5c. PROGRAM ELEMENT NUMBER | |
| 6. AUTHOR(S) | | | | 5d. PROJECT NUMBER 3058 | |
| | | | | 5e. TASK NUMBER RF9A | |
| | | | | 5f. WORK UNIT NUMBER | |
| 7. PERFORMING ORGANIZATION NAME(S) AND ADDRESS(ES) Air Force Research Laboratory (AFMC) AFRL/PRS 5 Pollux Drive Edwards AFB CA 93524-7048 | | | | 8. PERFORMING ORGANIZATION REPORT | |
| 9. SPONSORING / MONITORING AGENCY NAME(S) AND ADDRESS(ES) Air Force Research Laboratory (AFMC) AFRL/PRS 5 Pollux Drive Edwards AFB CA 93524-7048 | | | | 10. SPONSOR/MONITOR'S ACRONYM(S) | |
| | | | | 11. SPONSOR/MONITOR'S NUMBER(S) | |
| 12. DISTRIBUTION / AVAILABILITY STATEMENT Approved for public release; distribution unlimited. | | | | | |
| 13. SUPPLEMENTARY NOTES | | | | | |
| 14. ABSTRACT | | | | | |
| 20030127 085 | | | | | |
| 15. SUBJECT TERMS | | | | | |
| 16. SECURITY CLASSIFICATION OF: | | | 17. LIMITATION OF ABSTRACT A | 18. NUMBER OF PAGES | 19a. NAME OF RESPONSIBLE PERSON Leilani Richardson |
| a. REPORT Unclassified | b. ABSTRACT Unclassified | c. THIS PAGE Unclassified | | | 19b. TELEPHONE NUMBER (include area code) (661) 275-5015 |

Standard Form 298 (Rev. 8-98)
Prescribed by ANSI Std. Z39.18

21 separate items enclosed

9A

MEMORANDUM FOR IN-HOUSE PUBLICATIONS

FROM: PROI (TI) (STINFO)

16 Mar 98

SUBJECT: Authorization for Release of Technical Information, Control Number: AFRL-PR-ED-TP-1998-067
P.A. Strakey and D. Talley " The Effect of Manifold Cross-Flow on the Discharge Coefficient of Sharp-
Edged Orifices"
(Statement A)

The Effect of Manifold Cross-Flow on the Discharge Coefficient of Sharp-Edged Orifices

P. A. Strakey* and D.G. Talley

Air Force Research Laboratory
10 E. Saturn Blvd., Edwards AFB, CA, 93524 peter_strakey@ple.af.mil

ABSTRACT

The objective of this study is to determine the effect of manifold cross-flow on the discharge coefficient and cavitation characteristics of sharp-edged orifices over a wide range of flow-rates, back-pressures and cross-flow velocities. The orifice geometries studied cover a range of orifice diameters, length to diameter ratios and orifice angles characteristic of impinging element liquid rocket injectors. Experimental results for an orifice angle of 90° with respect to the manifold are presented here. Along with the experimental effort, an analytical model is being developed. The model predicts the discharge coefficient for a sharp edged orifice over a wide range of flow regimes including cavitating and non-cavitating flow, and for a wide range of orifice geometries. The analytical model generally shows good agreement with the experimental data over the range of conditions studied here. The model also closely follows the experimental data for cavitating flow except when the orifice length to diameter ratio is small, in which case the model over-predicts the discharge coefficient.

INTRODUCTION

In many atomization applications, such as rocket injectors, the manifold used to deliver liquid to an orifice can introduce a component of velocity normal to the axis of the orifice flow. Previous studies have indicated that manifold cross-flow can affect the orifice discharge coefficient and cavitation characteristics [1,2]. The net result is a variation in the discharge coefficient and thus mass flowrate by as much as ^{50%}~~fifty percent~~ depending on flow conditions and orifice geometry. Such a profound change in flowrate of an individual orifice can have a detrimental effect on spray characteristics, including droplet size, spray angle and cone angle. Any significant change in the expected spray characteristics could lead to decreased injector performance and damage to a combustion chamber due to increased heat flux near the wall.

* To whom correspondence should be addressed.

DISTRIBUTION STATEMENT A
Approved for Public Release
Distribution Unlimited

Background

Very little work has been done in the past with respect to manifold cross flow effects on discharge coefficient. Northrup [1] studied the effects of cross-velocity on sharp-edged orifices at pressure-drops up to 100 psi and atmospheric back pressure with cross-velocities up to 20 ft/s. He found that the discharge coefficient decreased as cross-velocity increased. He concluded that cross-velocity should be held to a minimum to avoid degradation in spray quality. Nurick [2] also studied the effects of manifold cross-flow on sharp-edged orifices of various shape at a chamber back-pressure of 0.69 Mpa and a pressure drop of 0.14 Mpa using water. He found that increasing the cross-velocity component from 0.3 m/s to 5.5 m/s decreased the discharge coefficient by about 5-10%. He also found that the increased cross-flow created visible disturbances, described as a brushy appearance, in the jets emanating from the orifices. Andrews and Sabersky [3] experimentally investigated the effect of cross-flow velocity on the discharge coefficient of a circumferential slot formed between two sections of circular pipe. The working fluid was water and the maximum cross-velocity studied was 6 m/s. Over the range of slot Reynolds numbers studied by the authors, the discharge coefficient was found to vary by as much as 50% as cross-velocity was varied. The discharge coefficient was found to decrease as the manifold to slot velocity ratio was increased beyond a certain value. They concluded that the fraction of available dynamic head in the approaching cross-flow that was converted into pressure-drop across the slot was much less than one, and decreased with increasing cross-flow to slot velocity ratio. Rhode and coworkers [4] experimentally measured the discharge coefficient of a round hole drilled in the side of a circular pipe using air as the working fluid. They showed as much as an eight-fold decrease in discharge coefficient for high manifold Mach number and low pressure-drop configurations. They found that the discharge coefficient correlated with the velocity head ratio, which was defined as the ratio of orifice total pressure-drop to manifold cross-flow momentum, $1/2\rho U^2$. Discharge coefficient was found to increase with increasing velocity head ratio.

Most of the work that has been described has been limited to relatively low injection pressures and low back-pressures. Also, most of the previous studies have been limited to a single flow regime, ie. either cavitating or non-cavitating flow. Most of the existing data has been presented with very little explanation as to why the discharge coefficient is affected by the manifold cross-flow. This makes it very difficult to extrapolate data that has been

generated at low pressures, to the typical pressures found in internal combustion engines or liquid rocket engines. The present study involves an experimental effort to quantify the effects of manifold cross-flow over a wide range of flow-rates, back-pressures and orifice geometries typical of impinging type liquid rocket injectors. A one-dimensional, physically based model has been developed to help correlate the data. The model is not unlike other models that have been developed in the past which predict discharge coefficient for sharp edged orifices in the absence of a manifold cross-flow [5,6,7]. The present model utilizes the same basic fluid mechanics, but also accounts for the incoming manifold flow which is oriented at 90° with respect to the injector flow. Also, the present model has been expanded to predict discharge coefficient for both cavitating and non-cavitating flow.

Experimental

The experimental investigation was carried out at the Air Force Research Laboratory cold-flow injector characterization facility, a simplified schematic of which is shown in Figure 1. Water, which is used as a simulant for liquid oxygen, is stored and pressurized in a 1 m³ tank. The injector inlet flowrate is controlled with a throttling valve and measured with one of several turbine flowmeters arranged in parallel to cover a wide range of flowrates. Downstream of the injector, another turbine flowmeter measures the outlet flowrate and a back-pressure regulator maintains the injector fluid pressure. Fluid pressures of up to 13.79 MPa and manifold velocities up to 40 m/s may be produced in this manner. The injector, as illustrated in Figure 2, consists of an interchangeable stainless steel plate with a sharp-edged hole machined in the center of the plate. This is mounted against the fluid manifold, which contains a 6.35 x 6.35 mm square channel machined into the manifold. A plenum and screen at the inlet and exit of the manifold reduces the velocity before the flow enters the manifold in order to generate a reproducible flowfield at the entrance to the orifice. The distance from the manifold inlet screen to the orifice entrance is 63.5 mm or 10 manifold channel widths. The entire arrangement is secured inside an optically accessible pressure chamber which is rated to 13.79 MPa.

The orifices are either pilot drilled and reamed, or made by electrical discharge machining with a diameter tolerance of $\pm 13 \mu\text{m}$ and inlet edge radius to orifice diameter ratio of less than 0.003, ensuring a sharp edged inlet. Chamber pressure, orifice pressure-drop, and inlet and outlet flowrates are recorded by a 12 bit analog to digital conversion

board and the data is stored on a personal computer. Experiments are typically conducted by setting the fluid pressure and flowrates to a predetermined value, with the chamber pressure being gradually increased while the data acquisition system records flowrates and pressures. This allows for a large amount of data to be collected in a relatively short period of time. Manifold velocities are held constant to within $\pm 1.5\%$ during the experiment. The experimental error associated with the discharge coefficient measurement is limited by the accuracy of the flowmeters which is $\pm 0.5\%$. This translates to a ~~one to twenty percent~~ ^{7 to 20%} error-band on the discharge coefficient data, with the larger errors occurring at the low orifice flowrates and high manifold flows.

The manifold was operated in three basic configurations; 1) fluid enters the inlet port and exits the outlet port of the manifold, thus providing cross-flow, 2) fluid enters the inlet port and the outlet port is blocked so that all of the flow exits the orifice, providing a case of zero cross-flow, and 3) fluid enters both the inlet and outlet ports and all of the fluid exits the orifice, providing a case of symmetric zero cross-flow hereafter called dead-head flow. This last flow condition is analogous to many axisymmetric injector geometries that have been studied in the past.

For the present study, a range of operating conditions and orifice geometries typical of liquid rocket injectors was studied and are given in Table 1. Although the objective of this study is to characterize injector angles between 30° and 150° , only results for orifices oriented at 90° with respect to the manifold flow are presented here.

Analytical Modeling

One of the objectives of this study is to provide the injector designer with a means of predicting the effects of manifold cross-flow on the discharge coefficient of a sharp-edged orifice. To accomplish this, an analytical model was developed that predicts discharge coefficient as a function of operating parameters, injector geometry and fluid properties. The model is based on fundamental, quasi one-dimensional fluid dynamics.

The model performs an energy balance along a streamtube originating in the manifold at station 1, and terminating at the point where the fluid exits the orifice into the chamber, at station 2, as shown in Figure 3. The boundaries of the

streamtube are defined by the dashed lines in Figure 3. The streamtube defines a volume of the flowfield in which fluid only enters and exits from the end of the tube; no fluid crosses the sides.

The energy equation for the special case of steady, incompressible, irrotational, inviscid flow through the streamtube is known as the Bernoulli equation and is written as follows.

$$\frac{P_1}{\rho} + \frac{1}{2} V_1^2 = \frac{P_2}{\rho} + \frac{1}{2} V_2^2 \quad (1)$$

Eq. (1) also assumes negligible effect of gravity which is appropriate where pressure forces and momentum greatly exceed the gravitational body forces. The problem with using Eq. (1) for the current application is that the flow through the manifold and orifice is both viscous and rotational, which introduces losses into Eq (1).

The main sources of losses in the flow are the loss of potential (pressure) and mean kinetic energy (velocity) to turbulence and friction (heat). To account for these losses, a modified energy equation is proposed as follows;

$$\frac{P_1}{\rho} + \frac{1}{2} \bar{V}_1^2 - E_{turb} - E_{friction} = \frac{P_2}{\rho} + \frac{1}{2} V_2^2 \quad (2)$$

Eq. (2) is similar to the approach taken by He and Ruiz [6] for modeling the discharge coefficient of a sharp-edged orifice at the point of cavitation inception in the absence of manifold cross flow. In Eq. (2), $E_{friction}$ accounts for the loss of energy from the mean flow due to viscous shear at the orifice walls and is modeled with a classical turbulent pipe flow friction loss term, which does an adequate job of correlating the data.

$$E_{friction} = f \frac{L}{D} \frac{V_2^2}{2} \quad (3)$$

The Darcy friction coefficient, f , in Eq. (3) is taken to be 0.04, which is the maximum value for turbulent flow in a smooth wall tube [8]. Previous experimental measurements have shown that the level of turbulence in a sharp-edged orifice greatly exceeds the level of turbulence found in fully developed pipe flow and can be characterized with a friction factor of transitional turbulent flow [6].

Turbulence losses are believed to mostly occur downstream of the vena contraction where the flow is expanding and an adverse pressure gradient is encountered. It has been shown through experimentation that a great deal of turbulence is generated under these conditions. The turbulence losses are modeled with an analytic expression that has been verified by much experimentation to represent the losses due to the sudden expansion downstream of the vena contraction [8].

$$E_{turb} = \frac{V_c^2}{2} \left[1 - \frac{d^2}{D^2} \right]^2 = \frac{V_2^2}{2} \left[\frac{1}{C_c} \right]^2 [1 - C_c]^2 \quad (4)$$

In Eq. (4), "d" is the diameter at the vena contraction and "D" is the actual orifice diameter, while $C_c = d^2/D^2$. Substituting Eqs. (3) and (4) in Eq. (2) and solving for the orifice exit velocity, V_2 , yields the equation;

$$V_2 = \left\{ \frac{\left[\frac{P_1 - P_2}{\rho} + \frac{\bar{V}_1^2}{2} \right]}{\left[\frac{1}{2} \left(\frac{1}{C_c} \right)^2 (1 - C_c)^2 + \frac{1}{2} + \frac{f L}{2 D} \right]} \right\}^{\frac{1}{2}} \quad (5)$$

where the orifice exit velocity, V_2 , is assumed to be constant over the orifice cross section. The discharge coefficient is defined as;

$$C_d = \frac{V_2}{\sqrt{\frac{2(P_1 - P_2)}{\rho} + V_1^2}} \quad (6)$$

which is consistent with the definition of discharge coefficient for the experimental measurements. Note that this definition of discharge coefficient is based on the total dynamic head in the manifold approaching the orifice. The volumetric flowrate through the orifice is calculated by the following relation.

$$Q_{or} = V_2 \cdot A_{or} \quad (7)$$

Manifold Boundary Layer

Due to the presence of a turbulent boundary layer in the manifold, the average velocity and, therefore, momentum, of the fluid entering the orifice streamtube is somewhat less than the bulk flow velocity, V_1 . In Eq. (2), the average manifold momentum entering the streamtube, \bar{V}_1^2 , is needed in the overall energy balance. This is taken to be an estimate of the average velocity squared in the boundary layer that enters the orifice. To do this, it is assumed that the orifice is equivalent to a slot as wide as the manifold with a cross sectional area equal to the orifice. With this assumption, it is further assumed that the fluid entering the slot is distributed evenly within the width of the manifold, i.e., there are no 3-d effects from the side walls of the manifold. The manifold boundary layer velocity profile upstream of the entrance to the slot is calculated by a classical turbulent 1/7 power law function [9].

$$V(y) = V_1 \left\{ \frac{y}{0.16 \cdot x \cdot \text{Re}_x^{1/7}} \right\}^{1/7} \quad (8)$$

where the Reynolds number, Re_x , is based on the distance from the entrance of the manifold, x .

$$\text{Re}_x = \frac{V_1 \cdot x \cdot \rho}{\mu} \quad (9)$$

In Eq. (8), y is the distance from the bottom of the manifold as in Figure 3. Once the velocity profile has been calculated as a function of y , the distance to the top of the streamtube, y' , is calculated by solving the volumetric flowrate integral, Eq. (10).

$$Q_{or} = \int_0^{y'} V(y) \cdot w \cdot dy \quad (10)$$

Once y' is known, the average momentum entering the streamtube is calculated by integrating the velocity profile from zero to y' , as in Eq. (11).

$$\bar{V}_1^2 = \frac{1}{y'} \int_0^{y'} V^2(y) \cdot dy \quad (11)$$

Due to the implicit nature of the set of Eqs. (2) - (11), an iterative solution procedure is adopted in which the orifice flow rate, Q_{or} , is first estimated, then the boundary layer momentum, \bar{V}_1^2 , and orifice velocity, V_2 , can be calculated and used as the orifice flow rate for the second iteration. A solution is usually converged upon within several iterations.

Contraction Coefficient

Once the manifold velocity has been calculated, the next step is to calculate the contraction coefficient in the orifice which is a result of the flow separation at the entrance to the orifice. The approach taken here is to assume that the manifold and orifice can be approximated as two-dimensional slots as was done in the calculation of the boundary layer in the previous section. The streamlines of the flow into the slot are then analytically approximated by potential flow theory. Two-dimensional potential flow theory has been shown to work well in approximating the contraction coefficient for a sharp-edged orifice in the absence of cross-flow [5,7]. Also, it has been found in this investigation that potential flow calculations of the contraction coefficient of a two-dimensional slot does an adequate job of correlating the data. Only a brief description of the resulting equations is provided here, while a more detailed analysis is presented in the literature [10,11,12].

Figure 4 shows a diagram of the actual orifice geometry (Figure 4a) and the two-dimensional slot geometry (Figure 4b) with the slot modeled as a barrier on the downstream side of the flow (Figure 4c). The edge of the streamtube is shown as a dashed line in Figure 4c. The contraction coefficient is the width of the streamtube at the point of maximum contraction, normalized by the slot width, "a". For a two-dimensional slot, as with a circular orifice, the contraction coefficient is equal to the ratio of effective flow area to total slot (orifice) area. The independent variables are "a", "b", and "c" (the three geometrical variables), and V_1 . The dependent variables are V_3 , V_c and α , the angle of the jet. The solution for the velocity at the vena contraction, V_c , is given by Eqs. (12a) through (12e). Once a solution for V_c and V_3 has been obtained, the contraction coefficient, C_c , can be calculated using Eq. (13). The solution of the set of Eqs. (12) and (13) requires an iterative procedure since Eqs. (12a) and (12d) cannot be solved for explicitly in terms of V_c .

$$\begin{aligned}
 (a) \quad \frac{a}{b} &= F\left(\frac{V_1}{V_c}\right) - F\left(\frac{V_3}{V_c}\right) - \frac{V_1 - V_3}{V_c} \cdot G(\alpha) \\
 (b) \quad F\left(\frac{V}{V_c}\right) &= \frac{2}{\pi} \left(1 + \frac{V^2}{V_c^2}\right) \cdot \tanh^{-1}\left(\frac{V}{V_c}\right) \\
 (c) \quad G(\alpha) &= \frac{2}{\pi} \cos(\alpha) \cdot \ln\left(\cot \frac{\alpha}{2}\right) - \sin(\alpha) \\
 (d) \quad \frac{c}{b} &= H\left(\frac{V_3}{V_c}\right) - H\left(\frac{V_1}{V_c}\right) + \frac{V_1 - V_3}{V_c} \cdot G\left(\frac{\pi}{2} - \alpha\right) \\
 (e) \quad H\left(\frac{V}{V_c}\right) &= \frac{2}{\pi} \left(1 - \frac{V^2}{V_c^2}\right) \cdot \tan^{-1}\left(\frac{V}{V_c}\right)
 \end{aligned} \tag{12}$$

$$C_c = \frac{(V_1 - V_3) \cdot b}{a \cdot V_c} \tag{13}$$

In solving the set of Eqs. (12) and (13), it was found that for slot length to width ratio, c/a , greater than about one, the contraction coefficient is only a function of the slot to manifold velocity ratio, V_2/V_1 . As the slot to manifold velocity ratio is decreased, the size of the separation zone increases and thus the contraction coefficient decreases as shown in

Figure 5. Figure 5 also shows the asymptotic behavior of the contraction coefficient approaching $C_c = 0.61$ as the orifice to manifold velocity ratio is increased. If one were to solve Eqs. (12) and (13) for the simplified case where V_3 is equal to zero (ie, all of the flow in the manifold passes through the orifice), a contraction coefficient of $C_c = 0.61$ is uniquely obtained. This is the classical solution that has been used for many previous discharge coefficient models in which there is no manifold cross-flow. The previous models have also shown very good agreement between experiment and model which would indicate that two dimensional potential flow theory performs well, at least in situations where there is no manifold cross-flow [5,7].

Cavitation

Once the contraction coefficient has been calculated, the flowrate through the orifice can be determined by Eqs. (5) and (7). Once the flowrate is known, it can be determined whether or not the flow in the orifice is cavitating. Cavitation occurs when the local fluid pressure reaches the vapor pressure of the fluid. For the current configuration, the minimum fluid pressure occurs at the vena contraction where fluid velocity is at a maximum. The pressure at the vena contraction can never be less than the vapor pressure of the fluid because the fluid vaporizes in order to maintain the vapor pressure. In this fashion, the vapor bubble that is formed acts as a variable area nozzle which maintains a constant mass flowrate through the orifice in the cavitating regime.

In order to determine if cavitation is occurring in the orifice, it must first be assumed that cavitation is not occurring which allows for the calculation of the contraction coefficient and orifice exit velocity, V_2 , as outlined above. The local fluid pressure at the vena contraction can be calculated using Eq. (14).

$$P_{vena} = \rho \cdot V_2^2 \cdot \left\{ \frac{1}{2} \left(\frac{1}{C_c} \right)^2 (1 - C_c)^2 + \frac{1}{2} + \frac{1}{2} f \frac{L}{D} \right\} - \frac{\rho}{2} \left(\frac{V_2}{C_c} \right)^2 + P_2 \quad (14)$$

Eq. (14) is simply an application of the energy equation, Eq. (2), from station "c" at the contraction to station "2" at the orifice exit. If the calculated P_{vena} is equal to or less than the vapor pressure of the fluid, then cavitation is known to be occurring, and the pressure at the vena contraction is known to be equal to the vapor pressure. The velocity at

the vena contraction is calculated by applying the energy equation from station ① to station ② in Figure 3, assuming negligible turbulence and friction losses along the way. The assumption of negligible losses from station ① to station ② is appropriate due to the very short distance between the entrance of the orifice and the vena contraction, which usually occurs within one orifice diameter downstream. When the energy equation is solved, the expressions for V_c is as follows:

use the proper area

$$V_c = \left\{ \frac{2}{\rho} (P_1 - P_v) + \bar{V}_1^2 \right\}^{\frac{1}{2}} \quad (15)$$

The orifice exit velocity is related to the velocity at the vena contraction through the contraction coefficient as follows:

$$V_2 = V_c \cdot C_c \quad (16)$$

Experimental Results and Model Predictions

As shown in Table 1, a large amount of data was obtained over a wide range of operating conditions. Both cavitating and non-cavitating flow was observed. Figures 6 through 13 show both raw data in the form of plots of discharge coefficient versus cavitation parameter, P_{cav} , and a comparison ^{of} ~~between~~ experimental data and model prediction for a variety of operating conditions, orifice geometries and flow conditions. P_{cav} is defined as:

$$P_{cav} = \frac{P_1 - P_v}{P_1 - P_2} \quad (17)$$

where P_1 and P_2 are the experimentally measured fluid and back-pressures, respectively and P_v is the vapor pressure of the fluid at ambient temperature. The discharge coefficient is defined by Eq. (6).

The experimental data in Figure 6 shows a large decrease in discharge coefficient as cross-velocity is increased for both cavitating and non-cavitating flow. This is due to an increase in the size of the recirculation zone as the manifold to orifice velocity is increased. As the recirculation zone increases in size, the vena contraction decreases in size and the flow is further constricted. The one-half power dependence of discharge coefficient on P_{cav} for P_{cav} less than about 1.8 is indicative of cavitating flow. In this regime the flowrate through the orifice is constant and is independent of the chamber back-pressure. The model does an adequate job of predicting the discharge coefficient in both the cavitating and non-cavitating regimes. The scatter in the data about the prediction line in Figure 6 is within the limits of measurement accuracy, especially at the high manifold flowrates and low orifice flows, where the experimental error in discharge coefficient can be as much as +/- 10%.

Figures 7 and 8 indicate that the effect of cross-flow is diminished as P_1 ; ~~and~~ therefore, the pressure-drop ΔP_0 is increased. This is due to the fact that the effect of cross-velocity on ^{the} contraction coefficient decreases with increasing orifice pressure and flowrate. The contraction coefficient remains constant at about 0.61 for orifice to manifold velocity ratios greater than three. Also, at the higher fluid pressures, the manifold dynamic head is small with respect to the static pressure-drop across the orifice.

Figure 9 shows the same trend in decreasing discharge coefficient as cross-velocity is increased for a length to diameter ratio of five, but also shows an increase in sensitivity ^{to} of the discharge coefficient to the manifold cross-velocity. This is due to the decreased frictional resistance of the shorter orifice. As the orifice length is increased, the effects of manifold flow on discharge coefficient are diminished due to the relative increase in frictional resistance. Figure 10 demonstrates the effect of orifice L/D ratio on discharge coefficient for both ^{the} experiment and ~~the~~ model and also lends credibility to the pipe flow frictional correlation used in the model.

The decrease in discharge coefficient with increasing manifold velocity is consistent with the findings of other researchers with similar experimental configurations [1-4]. A comparison ^{of} between data collected in the present study ^{with} and data collected by Nurick *et al.* [2] is shown in Figure 11, which is a plot of discharge coefficient versus manifold velocity. The data collected by Nurick *et al.* was for a L/D ratio of six, which was slightly longer than the

L/D ratio studied here ($L/D=5$). ^{although} The orifice diameters were also slightly different, ~~however~~, the orifice pressure-drop was the same ($dP = 0.14$ MPa). It should also be pointed out that Nurick's definition of discharge coefficient was different from the present study, therefore, Nurick's data was recomputed by the authors using the discharge coefficient definition given by Eq. (6). The comparison shows the same trend in decreasing discharge coefficient with increasing manifold velocity. The differences in measured discharge coefficient could be, in part, due to the differences in L/D ratio.

Figures 12 and 13 show behavior of an orifice with an L/D ratio of three at fluid pressures of 3.45 MPa and 10.34 MPa, respectively. The shorter orifice results in a slightly larger discharge coefficient at low cross-flows due to the decreased frictional resistance of the orifice. The model does an adequate job of predicting the discharge coefficient for the shorter orifice, although the model begins to over-predict the discharge coefficient in the cavitating regime. This seems to indicate that the model is not taking into account an additional loss in the system. The losses could be a result of incomplete velocity profile development downstream of the recirculation zone for the shorter orifice. If the velocity profile does not have sufficient time to develop into a flat profile downstream of the recirculation zone, some of the flow momentum will not be recovered in the form of potential energy, or pressure. This will result in a decreased discharge coefficient.

Figure 14 shows a comparison between the model prediction for the onset of cavitation and the experimentally measured cavitation inception point. As can be seen in the figure, the model shows an increase in P_{cav} at inception as the manifold velocity is increased at a fluid pressure of 0.69 MPa, and is consistent with the experimental data. The increase in P_{cav} at inception is due to a decrease in the contraction coefficient as cross-flow is increased, thus increasing the orifice velocity at the point of contraction and decreasing the pressure at this point. As the fluid pressure is increased to 3.45 MPa, the effect of cross-flow on cavitation inception is diminished due to the decrease in manifold to orifice velocity ratio. The cavitation inception point also decreases as the length to diameter ratio of the orifice is increased, as can be seen in Figure 12b. This is a result of the increased frictional resistance of the longer orifice which reduces the flowrate through the orifice. The reduced flowrate leads to lower velocities and hence higher pressures at the vena contraction which shifts the cavitation inception point to lower values of P_{cav} .

SUMMARY AND CONCLUSIONS

An experimental investigation was carried out to determine the effect of manifold cross-flow on the discharge coefficient and cavitation characteristics of sharp-edged orifices. The experiments were conducted over a wide range of flowrates, back-pressures, cross-flow velocities and orifice geometries characteristic of impinging element liquid rocket injectors. Experimental results for an orifice angle of 90° with respect to the manifold were presented. Discharge coefficient was found to decrease as manifold velocity was increased, due to an increase in the size of the recirculation zone just downstream of the orifice entrance. Discharge coefficient was also found to decrease with increasing orifice L/D ratio as a result of the increased frictional losses. Manifold cross-flow was also found to shift the point of cavitation inception to higher cavitation parameters, P_{cav} .

An analytical model was developed to predict discharge coefficient as a function of operating parameters and orifice geometry for both cavitating and non-cavitating flow. The model is based on a one-dimensional energy balance between the manifold and the orifice exit. Two-dimensional potential flow theory was used to calculate the effect of manifold flow on the contraction coefficient of the orifice. Turbulence production was modeled with an expression for flow losses from a sudden expansion and viscous losses at the orifice wall were accounted for with a pipe flow friction term. Cavitation was determined by calculation of the fluid pressure at the vena contraction and comparing this pressure to the vapor pressure of the fluid. The model was found to perform reasonably well in predicting both discharge coefficient and flow regime, i.e., cavitating or non-cavitating flow. The model does however show an over-prediction of discharge coefficient in the cavitating regime for L/D ratios of three. There appears to be some energy loss that the model does not account for. This could be due to reattachment effects downstream of the recirculation zone, such as a non-uniform velocity profile at the exit of the orifice.

Acknowledgment

The authors would like to thank Mr. Mike Griggs for his assistance in operating and maintaining the facility. Also, thanks go to Mrs. Julie Carlile and Ms. Lejui Pang for their assistance in overseeing facility engineering issues and for many hours spent collecting data.

REFERENCES

1. R.P. Northrup, Flow Stability in Small Orifices, *Proc. American Rocket Society, ASME*, 30 November, 1951.
2. W.H. Nurick and R.M. McHale, Noncircular Orifice Holes and Advanced Fabrication Techniques for Liquid Rocket Injectors, Final Report NASA CR-108570, Rocketdyne, Canoga Park, CA, October, 1970.
3. K.A. Andrews and R.H. Sabersky, Flow Through an Orifice from a Transverse Stream, *Transactions of the ASME*, vol. 112, Dec. 1990, pp. 524-526.
4. J.E. Rohde, H.T. Richards and G.W. Metger, Discharge Coefficient for Thick Plate Orifices With Approach Flow Perpendicular And Inclined to the Orifice Axis, NASA TN D-5467, October 1969, pp. 1-28.
5. F. Ruiz, A Few Useful Relations for Cavitating Orifices, *Proc. ICLASS-91*, pp. 595-602, Gaithersburg, MD, July 15-18, 1991.
6. L. He and F. Ruiz, Effect of Cavitation on Flow and Turbulence in Plain Orifices for High-Speed Atomization. *Atomization and Sprays*, vol. 5, pp. 569-584, 1995.
7. W.H. Nurick, Orifice Cavitation and its Effect on Spray Mixing, *Journal of Fluids Engineering*, pp. 681-687, December 1976.
8. Frank M. White, *Fluid Mechanics*, 2nd Ed., chap. 6, McGraw-Hill, New York, 1986.
9. T. Rogers and A.S. Hersh, Effect of Grazing Flow on Steady-State Resistance of Isolated Square-Edged Orifices, NASA Contractor Report, NASA CR-2681, April, 1976.
10. J.S. McNown and En-Yun Hsu, Application of Conformal Mapping to Divided Flow/*1st Midwestern Conf. on Fluid Dynamics*, pp 143-155, 1950.
11. R.V. Mises, Berechnung von Ausfluss und Ueberfallzahlen. *VDI Zeitschrift*, pp. 447-462, 1917.
12. Birkhoff and Zarantanello, *Jets, Wakes and Cavities, Applied Mathematics and Mechanics Vol. II*, McGraw-Hill, 1957.

NOMENCLATURE

| | | | |
|-----------|---|-------------|---|
| A_{ch} | manifold cross-sectional area (m^2) | Re_x | Reynolds number based on length |
| A_2 | orifice area (m^2) | Re_D | Reynolds number based on orifice diameter |
| C_c | contraction coefficient in orifice $\equiv d^2/D^2$ | Re_w | Reynolds number based on manifold width |
| C_d | discharge coefficient | V_1 | manifold cross velocity (m/s) |
| d | throat diameter at vena contraction (m) | \bar{V}_1 | average boundary layer velocity (m/s) |
| D | orifice diameter (m) | V_2 | orifice exit velocity (m/s) |
| E | energy per unit mass (J/kg) | V_c | velocity at vena contraction (m/s) |
| f | Darcy friction factor in orifice | V_3 | manifold velocity downstream of orifice (m/s) |
| L/D | length to diameter ratio of orifice | w | width of manifold (m) |
| P_1 | static pressure in the manifold (MPa) | x | distance from plenum to orifice (m) |
| P_2 | static pressure in the chamber (MPa) | y | distance from bottom of manifold (m) |
| P_v | vapor pressure of fluid (MPa) | | |
| P_{cav} | cavitation parameter | δ | boundary layer thickness (m) |
| P_c | pressure at the vena contraction (MPa) | ρ | density of fluid (kg/m^3) |
| Q_{or} | orifice flowrate (m^3/s) | μ | viscosity of fluid ($N\ s/m^2$) |
| | | α | orifice flow angle from manifold (degrees) |
| | | θ | orifice angle from manifold (degrees) |

LIST OF FIGURES

Figure 1 : Experimental facility.

Figure 2 : Fluid manifold.

Figure 3 : Streamtube for calculation.

Figure 4 : Diagram of; (a) actual geometry, (b) 2-d infinite slot geometry and, (c) 2-d potential flow theory geometry.

Figure 5 : Analytical solution from two-dimensional potential flow theory for contraction coefficient, C_c , as a function of slot to manifold velocity ratio, V_2/V_1 .

Figure 6 : Experimental data and model prediction for $D=1.19$ mm, $L/D=10$, $P_1=0.69$ MPa.

Figure 7 : Experimental data and model prediction for $D=1.19$ mm, $L/D=10$, $P_1=3.45$ MPa.

Figure 8 : Experimental data and model prediction for $D=1.19$ MPa, $L/D=10$, $P_1=10.34$ MPa

Figure 9 : Experimental data and model prediction for $D=2.03$ mm, $L/D=5$, $P_1=0.69$ MPa.

Figure 10 : The effect of orifice L/D ratio on discharge coefficient. $P_1=0.69$ MPa, $D=2.03$ mm, $P_{cav}=5$.

Figure 11 : Comparison of discharge coefficient data collected in the present study with data collected by Nurick *et al.*

Figure 12 : Experimental data and model prediction for $D=2.03$ mm, $L/D=3$, $P_1=3.45$ MPa

Figure 13 : Experimental data and model prediction for $D=2.03$ mm, $L/D=3$, $P_1=10.34$ MPa.

Figure 14 : Comparison of experimental data with model prediction for the onset of cavitation as a function of manifold velocity for a) $L/D=5$ and b) $L/D=10$.

LIST OF TABLES

Table 1 : Parameter ranges studied.

Table 1

| | |
|---|--|
| orifice diameter (mm) | 1.19 - 2.03 |
| length to diameter ratio | 3 - 10 |
| fluid pressure(MPa) | 0.69 - 10.34 |
| back-pressure(MPa) | 0.09 - 10.34 |
| cross-velocity (m/s) | 0 - 18.5 |
| orifice Re_D | $1.0 \times 10^4 - 3.0 \times 10^5$ |
| manifold Re_w | $6.0 \times 10^3 - 1.1 \times 10^5$ |
| manifold dynamic head to orifice static dP ratio | $5.0 \times 10^{-5} - 6.0 \times 10^0$ |

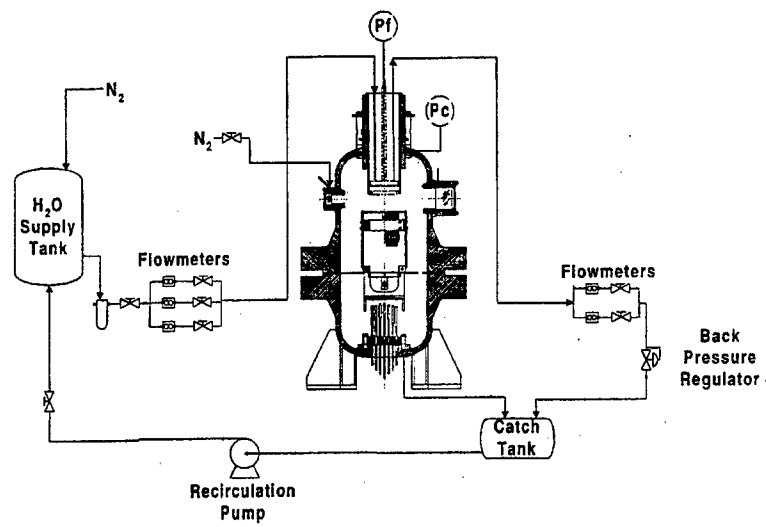


Figure 1

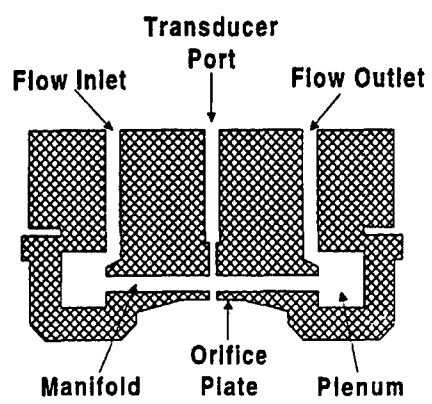


Figure 2

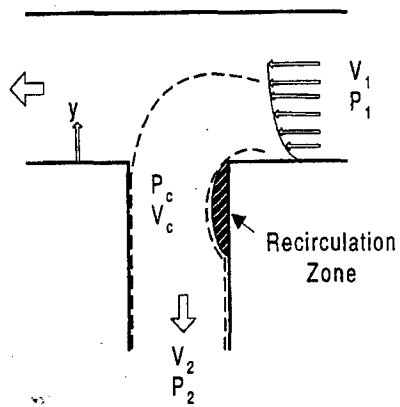


Figure 3

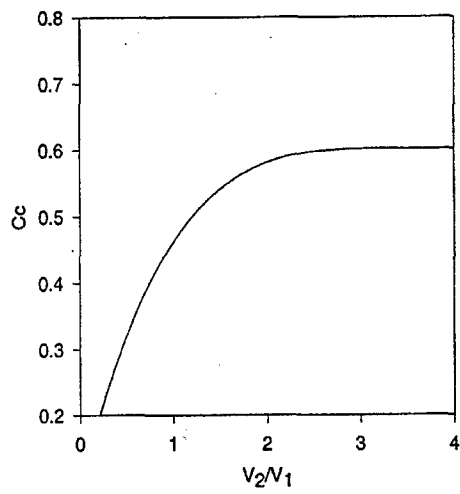


Figure 5

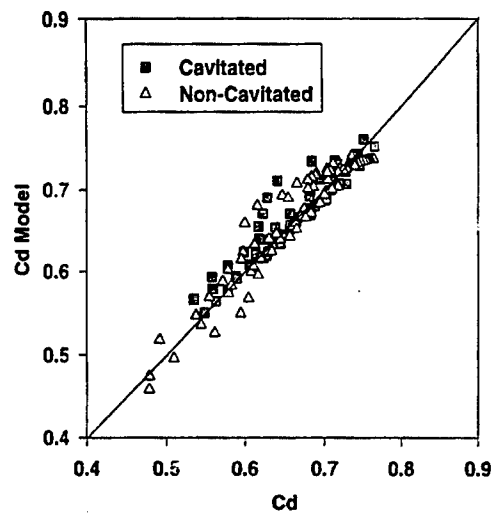
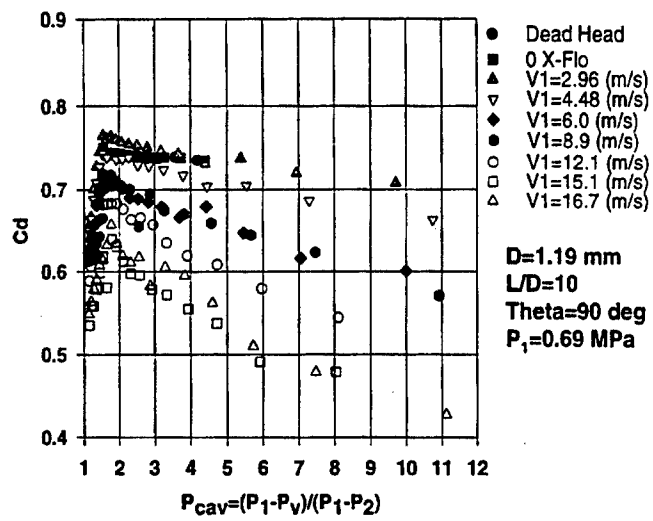


Figure 6

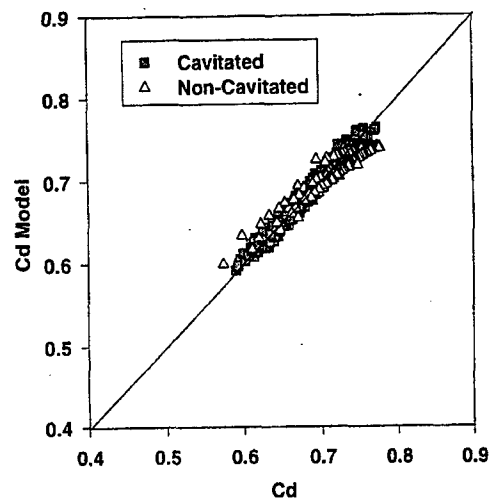
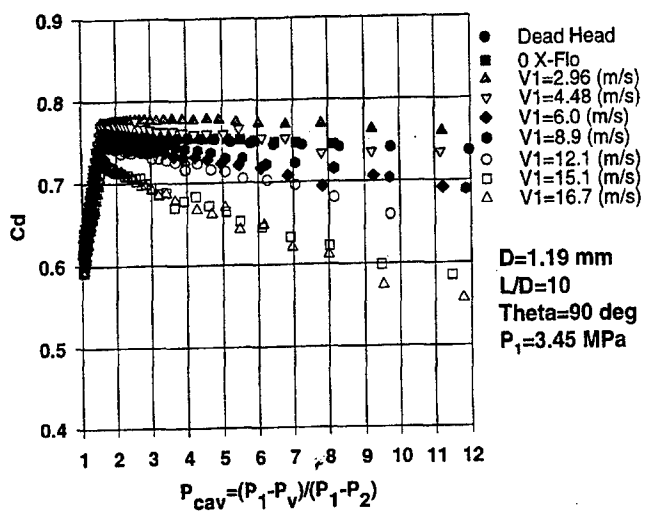


Figure 7

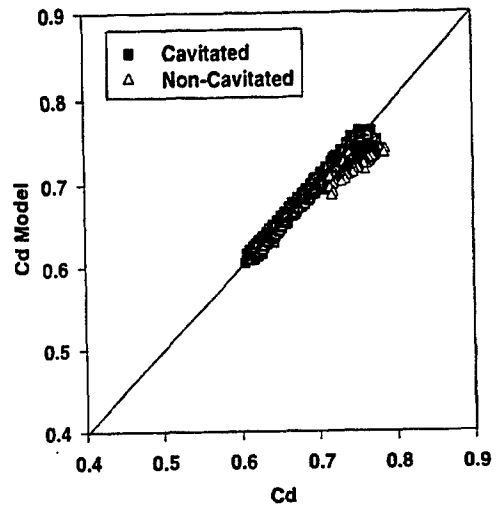
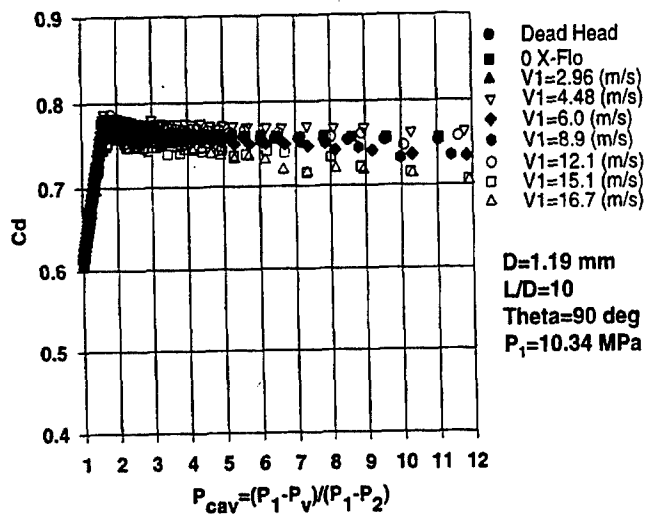


Figure 8

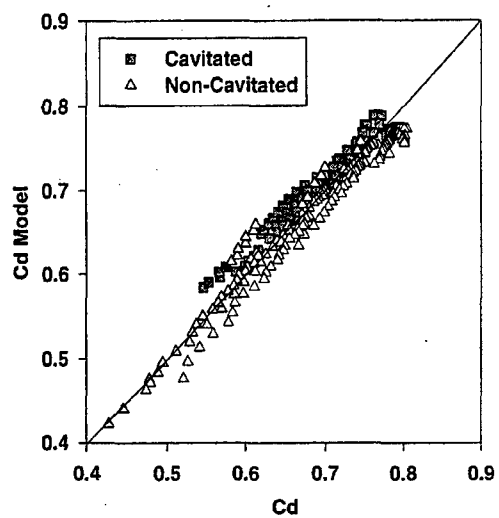
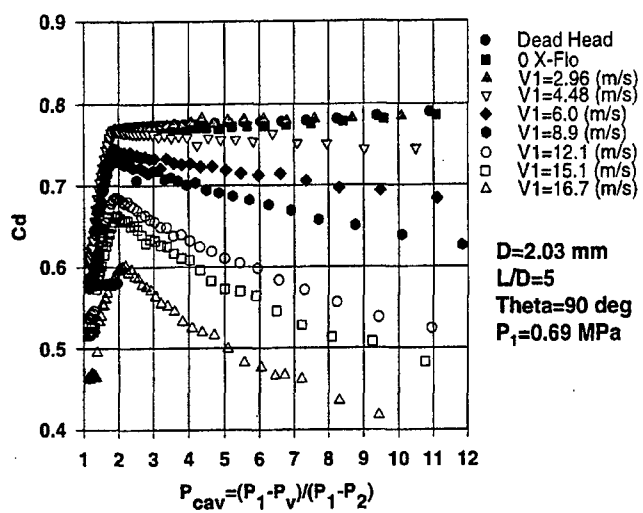


Figure 9

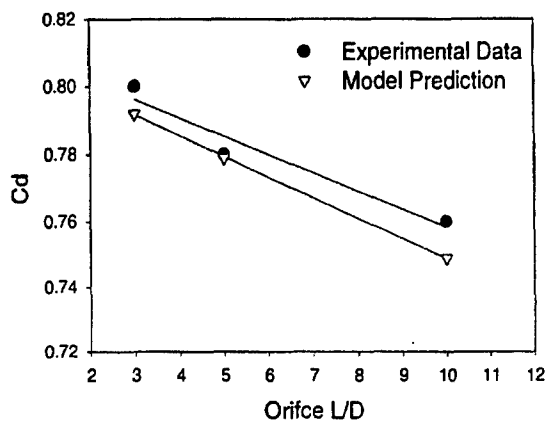


Figure 10

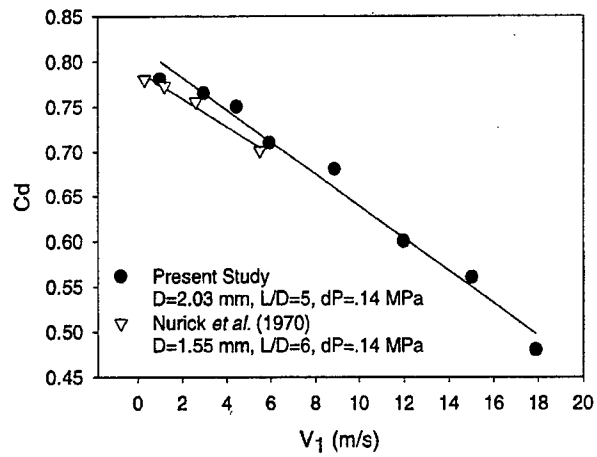


Figure 11

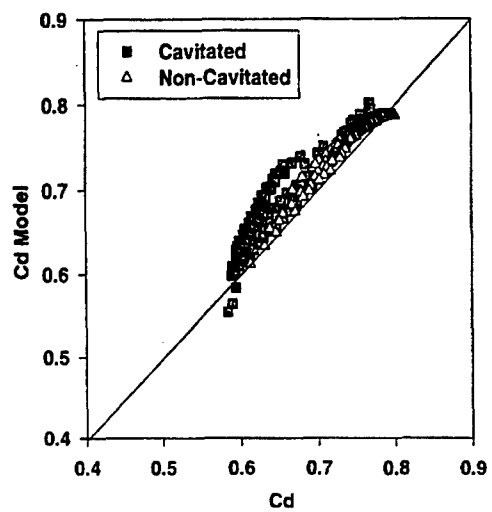
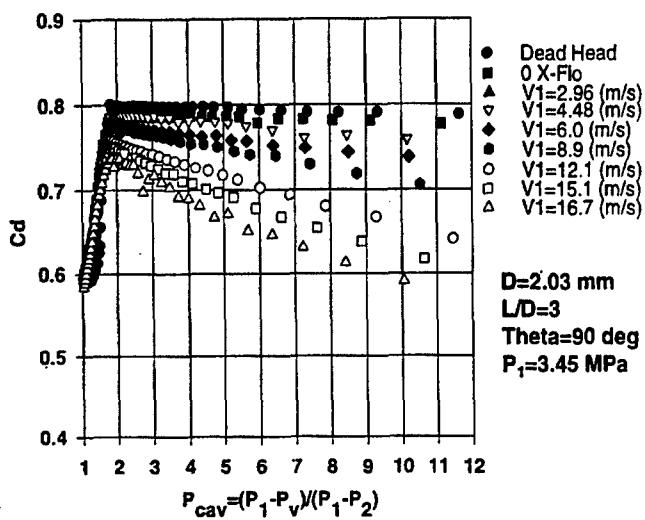


Figure 12

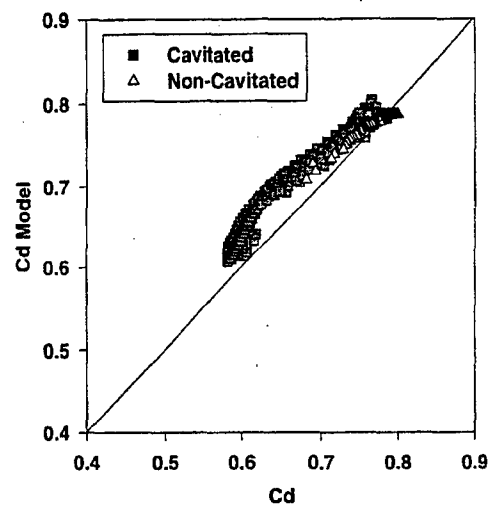
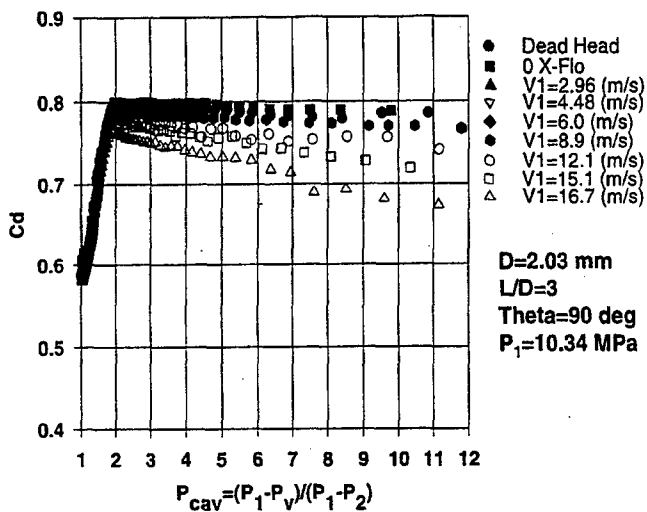


Figure 13

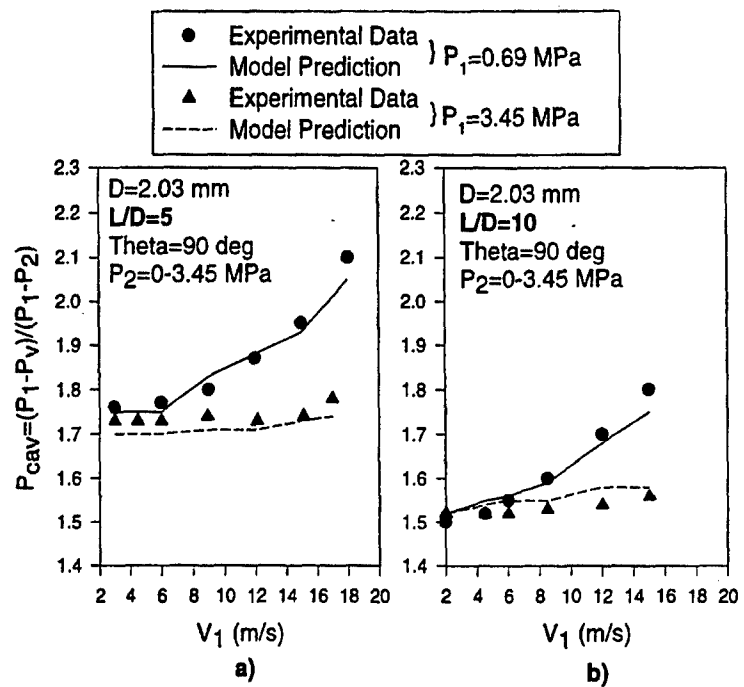


Figure 14